

Training Free Zero-Shot Visual Anomaly Localization via Diffusion Inversion

Samet Hicsonmez, Abd El Rahman Shabayek, Djamila Aouada
 University of Luxembourg, Luxembourg

{samet.hicsonmez, abdelrahman.shabayek, djamila.aouada}@uni.lu

Abstract

Zero-Shot image Anomaly Detection (ZSAD) aims to detect and localise anomalies without access to any normal training samples of the target data. While recent ZSAD approaches leverage additional modalities such as language to generate fine-grained prompts for localisation, vision-only methods remain limited to image-level classification, lacking spatial precision. In this work, we introduce a simple yet effective training-free vision-only ZSAD framework that circumvents the need for fine-grained prompts by leveraging the inversion of a pretrained Denoising Diffusion Implicit Model (DDIM). Specifically, given an input image and a generic text description (e.g., "an image of an [object class]"), we invert the image to obtain latent representations and initiate the denoising process from a fixed intermediate timestep to reconstruct the image. Since the underlying diffusion model is trained solely on normal data, this process yields a normal-looking reconstruction. The discrepancy between the input image and the reconstructed one highlights potential anomalies. Our method achieves state-of-the-art performance on VISA dataset, demonstrating strong localisation capabilities without auxiliary modalities and facilitating a shift away from prompt dependence for zero-shot anomaly detection research. Code is available at <https://github.com/giddyyupp/DIVAD>.

1. Introduction

Image Anomaly Detection (AD) focusses on the identification and localisation of abnormal regions within images. It plays a critical role in numerous computer vision applications. For instance, in quality inspection for manufacturing, early detection of defects ensures product integrity and helps reduce operational costs [4, 51, 65]. Current unsupervised AD methods train models using all the available normal images in a dataset. However, collecting large numbers of normal data still requires careful inspection. Moreover, for each new object class, the data collection and model training should be conducted again. In order to reduce the

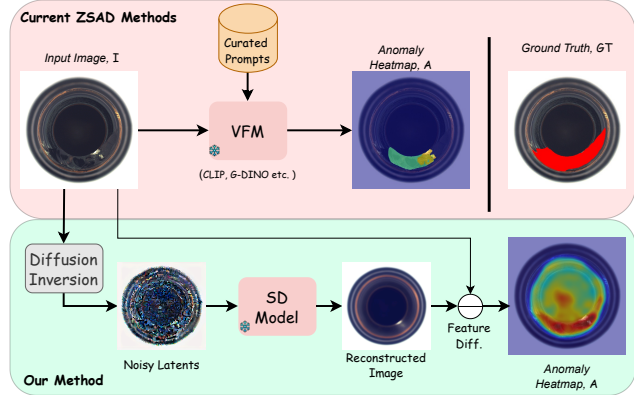


Figure 1. **An overview of the current training-free ZSAD methods vs DIVAD.** Current methods utilize pretrained large Vision Foundation Models (VFM) with specially curated object specific *guided-prompts*. Our method is free from any prompt tuning, and makes use of pretrained Stable Diffusion (SD) model to first invert a given image, and then reconstruct it through denoising.

data collection need, few-shot AD methods [28, 33] are proposed where the methods are trained using even as few as a single normal image, but they still train a separate model for each new class.

Zero-shot AD (ZSAD) takes one step further and does not require any data collected from the target dataset. Current ZSAD methods [8, 9, 11, 28, 34, 62] could be grouped into two categories: a) cross-data training based, b) training-free. The former category utilises a fully annotated dataset (e.g., MVTec-AD [5]) to train a model and test the trained model on the target dataset (e.g., VISA [65]). This approach assumes the availability of a closely related dataset with extensive annotations. Furthermore, these training-based methods utilise additional modalities such as text and generally require extensive domain knowledge to generate the initial set of guided prompts to define both normality and abnormality. Most of the time, the guided prompts are curated using the already labelled target test sets. Similarly, except for a few works, e.g., [48], training-free ZSAD methods heavily rely on extensive domain knowledge to define, especially, the abnormality to extract

useful textual features. For instance, WinCLIP [28] relies on over 1,000 handcrafted text prompts to achieve meaningful results, while AnomalyVLM [9] directly utilises label information from the target test set to construct anomaly prompts.

As a prominent approach for AD, reconstruction-based methods [3, 17, 22, 58] utilise Generative Adversarial Networks (GANs) [18] or diffusion models [27, 50]. Although these methods achieve very competitive performance, 1) they require large training sets, and 2) they train the models for long schedules, e.g., 1000 epochs for DiaD [22]. Another recent method, MAEDAY [48], proposes using a pre-trained Masked Auto-encoder to directly reconstruct a given image. However, their performance lags far behind that of current training-free ZSAD methods. Similar to MAEDAY, in our work, we directly use a pretrained diffusion model to reconstruct the given images for ZSAD with a novel formulation.

Our work is based on exploiting image inversion techniques. Inversion [16, 24, 39, 50] of an image using diffusion models means finding an initial latent noise vector that produces the input image. Specifically, Denoising Diffusion Implicit Models (DDIM) inversion [50] uses DDIM sampling in the reverse order, i.e., adding noise to the input image. In order to find the corresponding noisy latent vector, the inversion should be run with a large number of time steps, such as 1000. However, for efficiency, inversion is run for a few timesteps (e.g., 50), and sampling is done starting from an intermediate step (e.g., 20) to end up with almost the same image as the input. Usually, the inversion process requires a simple text prompt describing the input image.

In this work, we propose a simple training-free method utilising Diffusion Inversion for Visual Anomaly Detection, dubbed as DIVAD. It does not rely on any prompt generation or guidance and utilises the diffusion inversion mechanism to reconstruct a given input image. As the diffusion model is trained to generate normal looking samples, the inversion process generates the *normal version* of the input. The difference between the input and the inverted image denotes the locations of anomalies.

The proposed DIVAD has the following key contributions:

- We propose a training-free ZSAD method that utilises diffusion inversion at its core.
- Our method does not require any domain knowledge to design special guided prompts, nor require any anomaly definitions.
- DIVAD achieves state-of-the-art results on the VISA and MPDD datasets and on-par performance on MVTec-AD compared to current training-free ZSAD methods.

2. Related Work

2.1. Visual AD

Existing visual AD methods generally fall into three categories: embedding-based, augmentation-based, and reconstruction-based approaches.

Embedding-based methods extract image or patch features using pretrained networks and then compare these features between normal and anomalous samples to identify anomaly pixels. Early work [40] clustered features from ResNet [23] pretrained on ImageNet [15]. Subsequent methods [12, 14, 31, 46] introduced memory banks to provide richer feature contexts. Flow-based approaches [21, 32] model the distribution of normal patch features or minimise distances between positive samples. Knowledge distillation is also used, where a student network learns to replicate a teacher model trained on normal data [6, 52].

Augmentation-based methods simulate anomalies by applying corruptions or noise to normal images [57, 61] or their extracted features [37, 49]. For example, DRAEM [57] uses Perlin noise [41] to generate synthetic anomalies and trains an autoencoder to reconstruct both clean and corrupted images, while a discriminator highlights abnormal regions.

Reconstruction-based methods learn to generate normal versions of inputs using models such as VAEs [4], GANs [3, 47], vision transformers [59], and, more recently, diffusion models [22, 25, 54, 56, 58]. During inference, these methods rely on the assumption that anomalies will lead to higher reconstruction errors. For example, Bergmann et al. [4] showed that VAEs trained with an SSIM loss can detect pixel-level defects, while GANomaly [3] uses a GAN to detect image-level anomalies. ViTAD [59] integrates vision transformers into a VAE framework and achieves state-of-the-art results.

All these methods require a large labelled dataset, and most of them train for very long epochs to achieve satisfactory results.

2.2. Zero-Shot visual AD

ZSAD methods use extensive language guidance with the help of domain knowledge. They can be categorised into two groups: a) cross-data training-based methods and b) training-free methods.

Cross-data training based methods utilise an external fully labelled dataset with both normal and anomaly samples to train a model. These methods [8, 11, 20, 34, 62] make use of pretrained large-scale Vision Language Models (VLMs) [43]. They use frozen image encoders and make use of prompt learning strategies to inject additional tokens into text encoders to better represent normality and abnormality. AnomalyCLIP [62] introduces 12 separate object-agnostic learnable text prompt templates to represent both

normal and abnormal data. They train the model on the test sets of external datasets and evaluate it on the target test set. Similarly, FiLo [20] creates learnable prompts but guides the training with a possible anomaly location extracted using Grounding DINO [36]. The detected anomaly location is fed to both the anomaly prompts in the form of bounding box representation and to the visual encoder to focus on this region only. AdaCLIP [8] extends the idea of learnable text tokens to learnable image tokens. Moreover, in addition to learnable static tokens that are common to all the images, they use frozen CLIP as a Dynamic Prompt Generator to extract image-specific class tokens, which are incorporated into the learnable tokens.

Training-free methods do not need any external datasets to train a model, however, they still heavily rely on domain-specific knowledge to devise guided prompts to extract the anomaly regions. WinCLIP [28] creates around 1000 text prompts to cover every possible anomaly definition. Moreover, it uses label information (e.g., broken, contaminated, cracked) available in the dataset, which requires a domain expert to annotate, to generate the guided prompts. ALFA [63] uses a pretrained LLM to generate class-specific normal and abnormal prompts. They query a given test image to the LLM with the prompt, *Describe what a normal/abnormal image of [cls] looks like?* to extract the definitions. These LLM prompts are then directly used without any learning in the WinCLIP-like pipeline. AnomalyVLM [9] proposes a two-stage approach: first, the possible anomaly regions (bounding boxes) are extracted using Grounding DINO along with domain expert guided textual prompts, and then they use Segment Anything (SAM) [30] to segment the anomalies in this region using heuristics.

Different from previous methods, MAEDAY [48] does not rely on any textual input. They use a plain Masked Auto Encoder (MAE) trained on ImageNet [15]. During inference, they mask a large portion of an input image and let MAE fill in the masked regions to generate a complete image. Finally, the difference between the input and the reconstructed image denotes the anomalous regions.

Our method follows a similar approach and does not require any form of expert-generated text prompts. DIVAD reconstructs the input through DDIM inversion and calculates the pixel-wise feature differences between the input and generated images to segment the anomalous regions.

2.3. Diffusion Inversion

Latent vector manipulation based image editing has been successfully applied in GAN-based methods through inversion [1, 2, 7, 19, 55, 64]. Recently, the same approach is employed for diffusion methods [13, 16, 24, 39] and achieves remarkable performance. The goal of diffusion inversion is to manipulate a given image by changing desired parts of the input prompt, e.g., replacing a cat with a dog. The

very first DDIM or DDPM-based inversion [16] falls short when a big guidance value is used as the predicted noise with the input prompt, and denoising with the edited prompt diverges based on the strength of the parameter. Null text inversion [39] overcomes this issue by minimising the predicted noise with the input prompt and an empty prompt by optimising the empty text condition. Prompt-to-prompt [24] decides which parts of the image should be edited based on the input and edited prompts by checking the attention maps. DiffEdit [13] takes a similar approach and generates a mask to decide where the editing should happen. SDEdit [38] directly adds gaussian noise to the given stroke painting image, and then denoises it using a finetuned diffusion model to generate the corresponding color image.

Our approach is similar to the SDEdit process, where we add sampled noise to the input image latent and denoise it. However, in our case, there is no user guidance in any form.

3. Method

3.1. Problem Definition

For a given image $I \in \mathbb{R}^{H \times W \times C}$, Visual AD aims to perform 1) image-level classification and 2) pixel-level segmentation of anomalies. In this work, we focus on developing a training-free ZSAD method which **does not have any learnable parameters and does not require any labelled images**. Moreover, the method should be category-agnostic, i.e. not requiring any adaptation based on the characteristics of a specific object type.

3.2. Preliminaries

This section provides an overview of the core components and terminology related to text-guided diffusion models, including the denoising objective, classifier-free guidance, and DDIM inversion. These concepts form the foundation for our proposed approach and are essential for understanding the methodology presented in subsequent sections.

Text-Guided Diffusion Models. Text-conditioned diffusion models aim to synthesize images by progressively refining a noise vector z_t into an output image z_0 , guided by a textual prompt \mathcal{P} . The denoising network ϵ_θ is trained to predict the added noise ϵ , following the objective:

$$\min_{\theta} \mathbb{E}_{z_0, \epsilon \sim \mathcal{N}(0, I), t \sim \text{Uniform}(1, T)} \|\epsilon - \epsilon_\theta(z_t, t, c)\|^2, \quad (1)$$

where $c = \phi(\mathcal{P})$ is the embedding of the text condition, and z_t is a noisy version of a clean latent sample z_0 , obtained by perturbing it with gaussian noise at timestep t . During inference, starting from pure noise z_T , the model progressively denoises the latent through T iterative steps using the trained network.

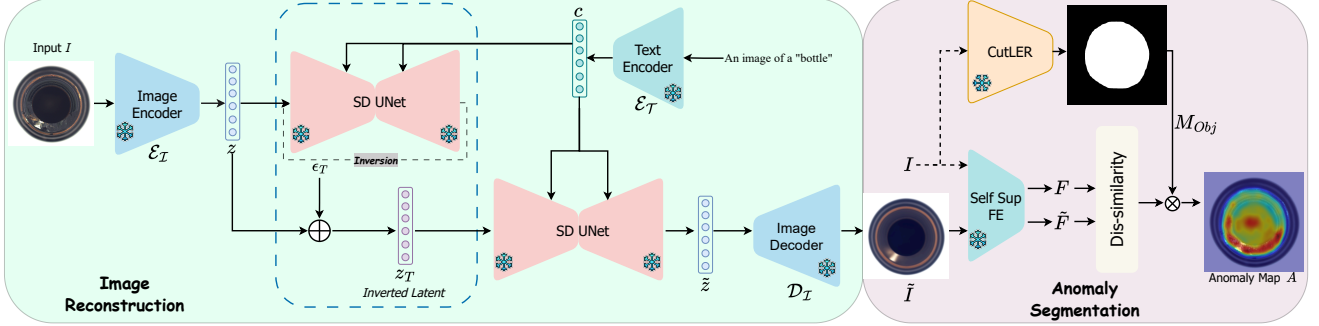


Figure 2. **The processing pipeline of DIVAD.** Given test image first encoded to latent representation, the SD UNet [45] predicts the noise ϵ_T for T timesteps using *DDIM Inversion* process. Predicted noise is added to the input image latent z to obtain inverted latent z_T . Then, this inverted latent is fed to the SD UNet model for denoising. Denoised latent is forwarded to the image decoder to recover a clean normal image. Instead of pixel wise comparison of input and reconstructed images which generates noisy regions, we perform segmentation on feature-level by utilizing a self-supervised model. Additionally, we make use of an object segmenter (CutLER [53]) to improve the segmentation performance.

To enable accurate reconstruction of real images, we adopt deterministic DDIM sampling [50], which performs the following update:

$$z_{t-1} = \sqrt{\frac{\alpha_{t-1}}{\alpha_t}} z_t + \left(\sqrt{\frac{1}{\alpha_{t-1}} - 1} - \sqrt{\frac{1}{\alpha_t} - 1} \right) \cdot \epsilon_\theta(z_t, t, c). \quad (2)$$

Here, α_t represents the variance schedule.

Unlike traditional models operating in pixel space, we leverage the Stable Diffusion (SD) model [45], which conducts diffusion in a learned latent space. An image x_0 is first encoded into a latent vector $z = \mathcal{E}_I(x_0)$, processed via the diffusion model (i.e. noise addition and denoising using UNet), and then decoded back using $x_0 = \mathcal{D}_I(z)$.

Classifier-Free Guidance. To enhance the effect of the text conditioning during generation, Ho et al. [26] proposed classifier-free guidance. This approach interpolates between conditional (i.e. using a text prompt) and unconditional (i.e. using an empty text) denoising predictions. Let $\emptyset = \phi("")$ denote the embedding of an empty prompt and w be the guidance scale, then:

$$\tilde{\epsilon}_\theta(z_t, t, c, \emptyset) = w \cdot \epsilon_\theta(z_t, t, c) + (1 - w) \cdot \epsilon_\theta(z_t, t, \emptyset). \quad (3)$$

In practice, a typical value such as $w = 3.5$ is used for text-to-image generation in SD, which we also use in our experiments.

DDIM Inversion. To reconstruct a known image from its latent encoding, we employ DDIM inversion [16, 50]. Under the assumption that the underlying Ordinary Differential Equation process can be approximately reversed, the inver-

sion proceeds as follows:

$$z_{t+1} = \sqrt{\frac{\alpha_{t+1}}{\alpha_t}} z_t + \left(\sqrt{\frac{1}{\alpha_{t+1}} - 1} - \sqrt{\frac{1}{\alpha_t} - 1} \right) \cdot \epsilon_\theta(z_t, t, c). \quad (4)$$

This formulation mirrors the forward process in reverse, from a clean latent code z which is typically obtained by encoding a real image, toward a noisy latent z_T . This enables direct inspection and manipulation of real data within the diffusion framework.

3.3. DIVAD

We present the detailed structure of our method in Figure 2. As our method is training-free, we use only the test images of each dataset. The inference pipeline starts by feeding the input test image I to the SD image encoder \mathcal{E}_I of the pre-trained SD model. The image encoder extracts the latent code z for the input image. Then, the backward diffusion is applied T times in reverse to add noise to z to obtain z_T with a simple text description of the image in the form of *"an image of a [obj]"*. Here obj corresponds to the class label of the input image. This noisy latent corresponds to a vector which is responsible for generating the input image I . When the denoising process is applied T times to the z_T , normally we should end up with z . However, as the network introduces error during the reverse process and the employed classifier guidance, usually denoised z_T and z do not exactly match. Hence, there is a difference between the input image I and the generated image I_T from z_T . A common approach to achieve almost the same reconstruction is to start the inversion from a small T' . The noisy latent $z_{T'}$ is fed to the SD model for denoising again for T steps to obtain \tilde{z} . The denoised latent \tilde{z} is decoded back to the image space using the pretrained SD image decoder \mathcal{D}_I to get the reconstructed image \tilde{I} . In order to segment the

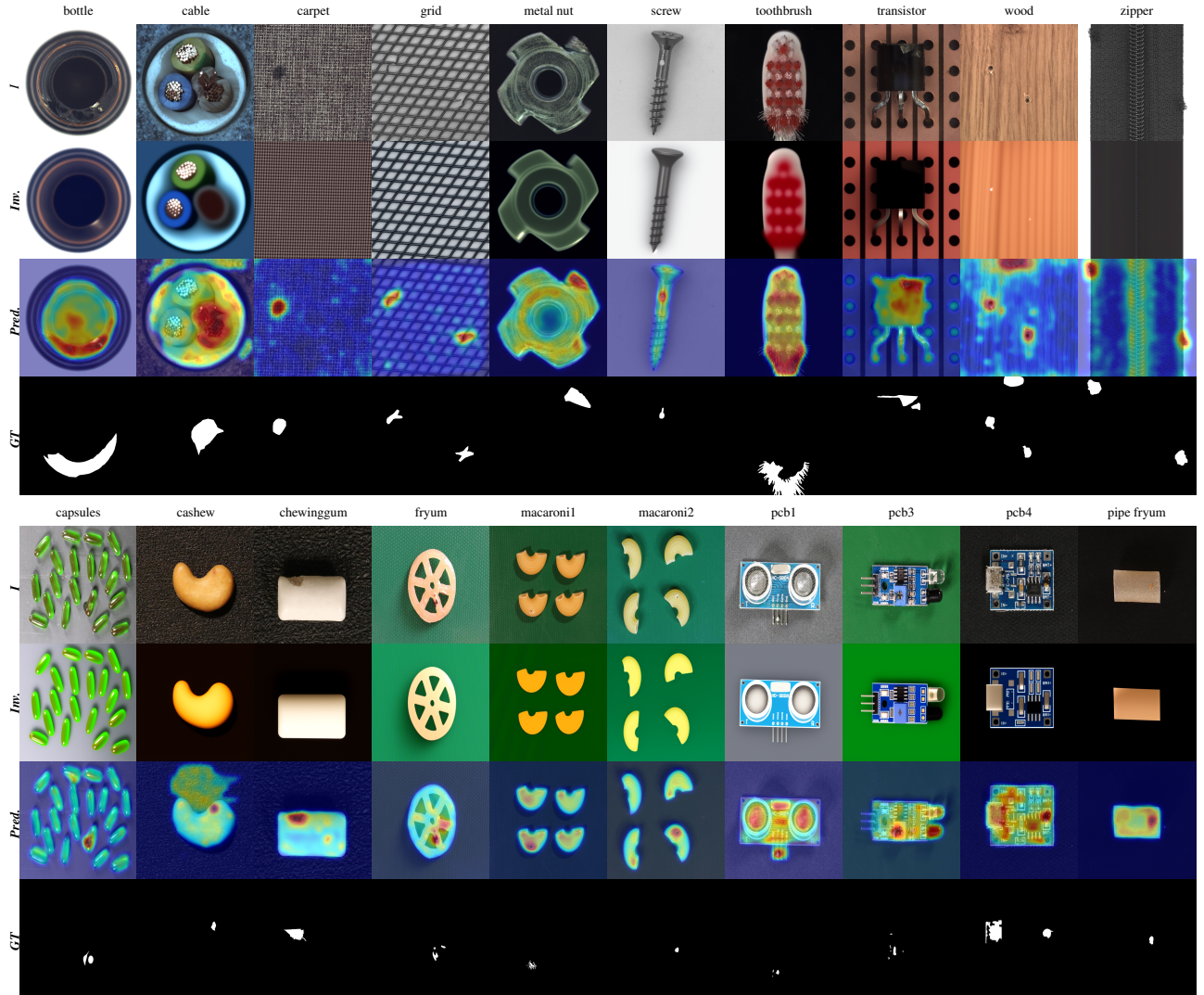


Figure 3. Qualitative results of DIVAD on MVTec-AD (top) and VISA (bottom) for selected classes. DIVAD successfully detects the anomaly locations on various object and texture classes.

Table 1. Details of the MVTec-AD and VISA test sets. Obj. stands for Object and Tex. stands for Texture categories.

Dataset	Categories		Images	
	Obj.	Tex.	Anomaly	Normal
MVTec-AD [5]	10	5	1,258	467
VisA [65]	12	N/A	962	1,200

anomaly locations, the input image I and the reconstructed image \tilde{I} are fed to an off-the-shelf self-supervised model (i.e., DINO [10]) to extract the features F and \tilde{F} , respectively. Finally, the pixels with high dissimilarity between these two feature vectors denote the Anomaly Map.

We observe that for some classes, there are irregularities in the background itself which need to be filtered out. To this end, we utilise a pretrained unsupervised image segmentation model CutLER [53] to extract the binary object mask(s) M_{Obj} of the input image I . The estimated mask is multiplied by the predicted anomaly map A to get the final segmentation mask.

4. Experiments

4.1. Datasets

MVTec-AD contains 10 "object" and 5 "texture" classes, with 1258 anomaly and 467 normal test images. The VISA dataset contains only "object" classes and has 962 anomaly and 1200 normal test images. Note that the VISA test

Table 2. Comparison of **ZSAD methods** on the **MVTec-AD** [5] and **VISA** [65] datasets. \dagger denotes methods without publicly available implementation. **N/A** means there is no evaluation on the specific dataset. In the **training-free** category, our method achieves on-par results compared to guided-prompt based methods on MVTec-AD, and outperforms all training-free ZSAD methods on pixel-level metrics on VISA dataset.

Method	Train	Guided Prompts	MVTec-AD					VISA				
			ROC_I	ROC_P	PRO	AP_P	$F1_P$	ROC_I	ROC_P	PRO	AP_P	$F1_P$
APRIL-GAN [11]	✓	✓	86.1	87.6	44.0	40.8	43.3	77.5	94.2	86.6	25.8	32.3
AnomalyCLIP [62]	✓	✓	91.5	91.1	81.4	34.5	39.1	80.9	95.5	86.7	21.3	28.3
FiLo [20]	✓	✓	91.4	93.1	61.7	52.2	52.0	83.9	95.9	85.4	31.4	38.5
PromptAD [34] \dagger	✓	✓	90.8	92.1	72.8	-	36.2	N/A	N/A	N/A	N/A	N/A
AdaCLIP [8]	✓	✓	89.9	89.9	44.0	41.6	43.9	86.2	95.8	51.0	31.5	37.1
Bayes-PFL [42]	✓	✓	92.3	91.8	87.4	48.3	-	87.0	95.6	88.9	29.8	-
DZAD [60] \dagger	✓	✗	93.5	86.7	-	-	-	90.2	92.0	-	-	-
WinCLIP [28]	✗	✓	91.8	85.1	64.6	18.2	31.6	78.1	79.6	56.8	5.4	14.8
ALFA [63] \dagger	✗	✓	93.2	90.6	78.9	-	36.6	81.2	85.9	63.8	-	15.9
FADE [35]	✗	✓	90.0	89.6	84.5	34.1	39.8	78.1	91.5	79.3	10.0	16.7
AnomalyVLM [9]	✗	✓	62.4	73.1	42.4	28.7	37.7	71.0	75.8	36.9	13.8	22.1
RAG [44] \dagger	✗	✓	92.5	89.1	-	-	-	86.8	87.6	-	-	-
MAEDAY [48] \dagger	✗	✗	74.5	69.4	-	-	-	N/A	N/A	N/A	N/A	N/A
DIVAD (ours)	✗	✗	76.0	88.6	73.3	31.6	35.7	69.7	93.4	78.2	19.5	24.0

split has a balanced number of normal and anomaly images. Since our method is training-free, we are not interested in the training statistics of the datasets. Details of both datasets are presented in Table 1.

4.2. Experimental Setup

We use the publicly available Stable Diffusion 2.1 weights ¹ for our pipeline. We use 50 for the reverse sampling timestep T , and 10 as the T' for the diffusion denoising starting point. For all datasets, images are resized to 256×256 pixels after reconstruction for inference. All the experiments are performed on a single Nvidia A100 GPU.

We use DINO ViTS/8 [10] as the feature extractor. We first extract patch features from the last layer for the input and reconstructed images, and then measure the cosine dissimilarity (i.e. $1 - \text{cossim}(\tilde{F}, F)$) between the patch features. The final heatmap is resized to the input size to locate the anomalies.

For object segmentation, we use an unsupervised model CutLER [53] with Cascade Mask R-CNN as the backbone detector. We set the confidence threshold as 0.1 and merge all the pixels above this threshold to use as object masks.

We run our method for 5 times on all datasets and observed only fractional differences which could be accounted for floating point operations. Our method consumes less than 7.5 GB of GPU memory and takes 5 seconds to find

the inverted latents and another 5 seconds to denoise the noisy latents on a single NVIDIA RTX A6000 GPU.

4.3. Qualitative Results

We show visual results of DIVAD in Figure 3 for the MVTec-AD (top) and VISA (bottom) datasets, respectively.

On MVTec-AD, our method effectively segments both object and texture categories across diverse defect types, including *broken*, *dent*, *color*, and *bent*. As illustrated in Figure 3 (top), representative examples include the *bottle*, *metal nut*, *carpet*, and *transistor* categories. Even large (e.g., *bottle*, *cable*) and multiple anomalies (e.g., *grid*, *wood*, *zipper*) are localised with high precision.

On VISA dataset, anomalies are often more subtle and appear in fine-grained details, making the detection task more challenging. Nonetheless, DIVAD demonstrates strong performance across various object categories with minor anomalies, such as *cashew*, *fryum*, and *macaroni*.

4.4. Quantitative Results

Metrics. Following common practice, we used five metrics: Mean Area under the ROC curve mAU-ROC [57] on image and pixel levels, pixel-level per-region-overlap *PRO* [6] score, $F1_P$, and average precision AP_P .

State-of-the-art comparison. DIVAD is compared with both training-based and training-free ZSAD methods. If the value for a metric is present in the original paper or offi-

¹huggingface.co/stabilityai/stable-diffusion-2-1

Table 3. Comparison of **training-free ZSAD methods** on the **MPDD** [29] dataset. Our method achieves SoTA results.

	ROC_I	ROC_P	PRO	AP_P	$F1_P$
WinCLIP [28]	61.4	71.2	53.4	6.7	15.4
FADE [35]	62.8	94.2	81.9	18.9	24.6
AnomalyVLM [9]	50.5	78.0	27.8	7.5	18.1
DIVAD	63.4	94.9	82.0	22.9	27.0

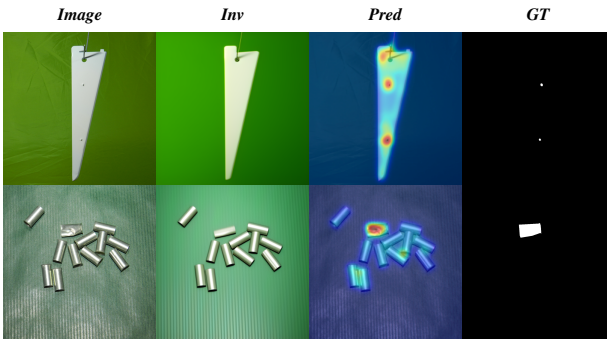


Figure 4. Examples of DIVAD predictions on the MPDD dataset.

cial repository, we directly use it. When available, we use official code or pretrained models to calculate the missing values.

MVTec-AD and VISA quantitative results are presented in Table 2. DIVAD achieves on-par results compared to training-free ZSAD methods on the MVTec-AD dataset. Similarly, on the VISA dataset, our method establishes state-of-the-art performance for pixel-level ROC , AP , and F_1 among training-free ZSAD methods. Furthermore, compared to the previous diffusion-based method DZAD [60] (the best performing on the image-level ROC among the training-based methods), DIVAD achieves better pixel-level scores without any training.

MPDD. In order to demonstrate the generalisation of DIVAD, we experimented with another challenging industrial defect dataset. We compare our method only to training-free ZSAD methods (c.f. Table 3), and DIVAD significantly improves the current state-of-the-art, especially on the pixel-level metrics. We present visual results of DIVAD in Figure 4 for selected classes. Detailed class-wise results on all datasets are available in the Supplementary Material.

4.5. Ablation Experiments

Effect of using object mask extraction (c.f. Table 4). In order to see the effect of using the extracted object masks (M_{Obj}), we calculate the performance of DIVAD with and without this step. As MVTec-AD contains both texture and object classes, we run separate experiments by enabling the

Table 4. Effect of using object segmentation method for object and texture classes.

Dataset	Obj. Mask		Metrics				
	Obj.	Tex.	ROC_I	ROC_P	PRO	AP_P	$F1_P$
MVTec-AD	✗	✗	77.5	85.7	76.8	33.5	36.5
	✓	✗	76.0	88.6	73.3	31.6	35.7
	✓	✓	70.9	79.9	57.6	23.0	29.1
VISA	✗	N/A	67.5	85.7	67.6	13.0	17.9
	✓	N/A	69.7	93.4	78.2	19.5	24.0

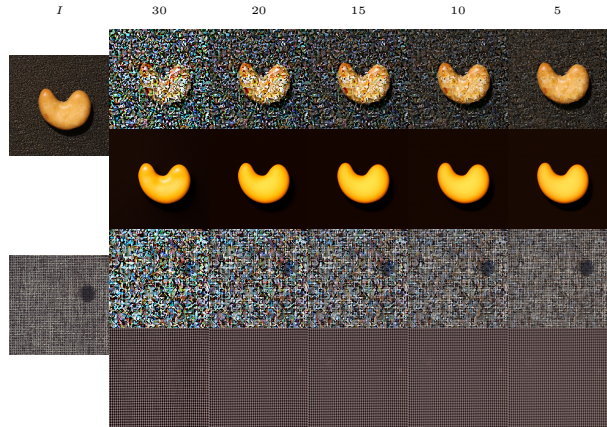


Figure 5. Diffusion inversion visuals for an object on the top and a texture on the bottom. Starting from a small T' captures more features from the input image as expected. A value between 10 and 15 achieves the best reconstruction.

mask extraction for each group.

On the VISA dataset, where there are only objects, using the object mask to refine the anomaly maps brings dramatic improvements. This is due to the fact that the background on this dataset has some irregularities, and they are detected as false positives by DIVAD.

On the MVTec-AD dataset, first of all, using the masks for the textures significantly reduces performance. This is expected since there is no dominant object; CutLER fails to segment the image. In our second experiment, we evaluate the impact of applying M_{Obj} to object categories. Consistent with the texture results, the use of object masks leads to a performance drop across all metrics except ROC_P . This decline is primarily attributed to categories with large anomalous regions such as *bottle* and *metal nut* where the segmentation model struggles to produce accurate object masks, thereby negatively affecting performance. Notably, the PRO metric decreases by approximately 20 points for both classes. In order to have a unified framework for both datasets, we report final results by using M_{Obj} on objects,

Table 5. Ablation experiments on the effect of varying the timestep and SD version.

Time step	SD vers.	MVTec-AD					VISA				
		ROC_I	ROC_P	PRO	AP_P	$F1_P$	ROC_I	ROC_P	PRO	AP_P	$F1_P$
30	1.5	70.9	87.7	71.1	28.0	33.6	64.0	92.4	74.3	15.6	19.2
20	1.5	72.2	87.9	72.5	30.0	34.8	69.1	93.4	77.8	18.4	23.4
15	1.5	74.2	87.9	72.5	30.7	35.2	69.4	93.4	78.1	19.5	24.1
10	1.5	74.4	87.8	72.2	30.8	35.2	70.2	93.4	78.3	19.7	24.4
5	1.5	73.9	87.2	70.9	30.5	35.4	71.1	93.3	78.2	19.7	24.6
30	2.1	72.5	87.9	71.1	28.1	33.1	65.8	92.5	74.6	14.9	18.6
20	2.1	74.4	88.0	72.8	31.0	35.4	68.2	93.5	78.0	18.3	23.0
15	2.1	75.1	88.0	72.6	31.0	35.4	68.7	93.5	78.2	19.5	23.9
10	2.1	76.0	88.6	73.3	31.6	35.7	69.7	93.4	78.2	19.5	24.0
5	2.1	75.3	87.5	71.4	31.0	35.9	70.1	93.3	78.2	19.2	23.9

Table 6. Relative change with an empty prompt during inversion.

Dataset	ROC_I	ROC_P	PRO	AP_P	$F1_P$
MVTec-AD	-1.5	-6.7	-14.6	-11.2	-9.3
VISA	-0.1	-0.7	-3.3	-1.0	-1.8

but not on textures.

Effect of varying the timestep. A critical hyperparameter in our method is to decide which timestep T' should be used for denoising when the reverse sampling timestep T is set 50. In Table 5, we present the quantitative results for changing T' from 30 to 5, i.e., reducing the added noise. See Figure 5 for examples of objects and textures. In both datasets, a T' value between 5 and 15 gives the best overall results. This result shows the importance of **starting the denoising from a less contaminated latent vector**.

Effect of changing SD version. Different SD versions were examined, specifically 1.5 and 2.1. On MVTec-AD, SD 2.1 achieved slightly better performance. Whereas on VISA, the best results are obtained with SD 1.5. In order to have a consistent version, we chose SD 2.1 and present the final results with it.

Effect of using empty text input. Our method only utilises the class name of the object as textual input. Although it requires no additional burden compared to deriving hundreds or even thousands of guided prompts, we ran experiments using an empty text as a condition to make it completely prompt-free. We present the relative change (c.f. Table 2) when we omit the text input in Table 6. On the VISA dataset, the difference is quite low, especially on the ROC metrics. However, on the MVTec-AD dataset, pixel-level metrics dropped significantly when no textual guidance is used, mainly due to the texture classes.

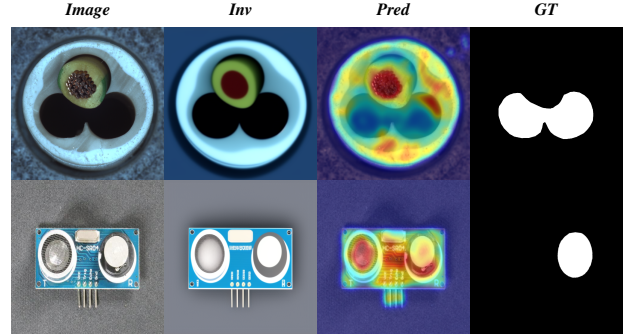


Figure 6. Example failure cases of DIVAD. Missing objects and contextual defects are not recoverable.

4.6. Limitations

Figure 6 shows a couple of failure cases. For example, in the top row, when the anomaly is a missing part of the object, the inversion process could not complete the missing area. Another example, in the bottom row, when the object has many small details, such as soldering and pins, the inversion fails to reconstruct a correct image. Furthermore, we observe that our ROC_I metric on MVTec-AD and VISA is lower than other baselines. This is due to the detection of anomalous pixels in images labelled as normal. These failures could be addressed by introducing a normal image example, which would extend our framework to few-shot based detection, a task we leave as future work.

5. Conclusion

Our method, DIVAD, highlights the potential of diffusion inversion as a powerful tool for ZSAD, offering a guided-prompt free, training-free, and vision-only alternative that achieves SoTA localisation performance on the VISA dataset. By eliminating the reliance on fine-grained

prompts or auxiliary modalities, our approach simplifies the ZSAD pipeline while maintaining competitive performance. This work not only broadens the applicability of diffusion models in anomaly detection but also paves the way for future research into leveraging generative priors.

Acknowledgments. This research was funded in whole or in part by the Luxembourg National Research Fund (FNR), grant reference DEFENCE22/17813724/AUREA.

References

- [1] Rameen Abdal, Yipeng Qin, and Peter Wonka. Image2stylegan: How to embed images into the stylegan latent space? In *ICCV*, pages 4432–4441, 2019. [3](#)
- [2] Rameen Abdal, Yipeng Qin, and Peter Wonka. Image2stylegan++: How to edit the embedded images? In *CVPR*, pages 8296–8305, 2020. [3](#)
- [3] Samet Akcay, Amir Atapour-Abarghouei, and Toby P Breckon. Ganomaly: Semi-supervised anomaly detection via adversarial training. In *ACCV*, pages 622–637, 2019. [2](#)
- [4] Paul Bergmann, Sindy Löwe, Michael Fauser, David Sattlegger, and Carsten Steger. Improving unsupervised defect segmentation by applying structural similarity to autoencoders. *arXiv preprint arXiv:1807.02011*, 2018. [1, 2](#)
- [5] Paul Bergmann, Michael Fauser, David Sattlegger, and Carsten Steger. Mvtac ad—a comprehensive real-world dataset for unsupervised anomaly detection. In *CVPR*, pages 9592–9600, 2019. [1, 5, 6](#)
- [6] Paul Bergmann, Michael Fauser, David Sattlegger, and Carsten Steger. Uninformed students: Student-teacher anomaly detection with discriminative latent embeddings. In *CVPR*, 2020. [2, 6](#)
- [7] Andrew Brock, Theodore Lim, JM Ritchie, and Nick Weston. Neural photo editing with introspective adversarial networks. In *ICLR*, 2017. [3](#)
- [8] Yunkang Cao, Jiangning Zhang, Luca Frittoli, Yuqi Cheng, Weiming Shen, and Giacomo Boracchi. Adaclip: Adapting clip with hybrid learnable prompts for zero-shot anomaly detection. In *ECCV*, pages 55–72, 2024. [1, 2, 3, 6](#)
- [9] Yunkang Cao, Xiaohao Xu, Yuqi Cheng, Chen Sun, Zongwei Du, Liang Gao, and Weiming Shen. Personalizing vision-language models with hybrid prompts for zero-shot anomaly detection. *IEEE Transactions on Cybernetics*, 2025. [1, 2, 3, 6, 7](#)
- [10] Mathilde Caron, Hugo Touvron, Ishan Misra, Hervé Jégou, Julien Mairal, Piotr Bojanowski, and Armand Joulin. Emerging properties in self-supervised vision transformers. In *ICCV*, pages 9650–9660, 2021. [5, 6](#)
- [11] Xuhai Chen, Yue Han, and Jiangning Zhang. April-gan: A zero-/few-shot anomaly classification and segmentation method for cvpr 2023 vand workshop challenge tracks 1&2. In *CVPRW*, 2023. [1, 2, 6](#)
- [12] Niv Cohen and Yedid Hoshen. Sub-image anomaly detection with deep pyramid correspondences. *CoRR*, abs/2005.02357, 2020. [2](#)
- [13] Guillaume Couairon, Jakob Verbeek, Holger Schwenk, and Matthieu Cord. Diffedit: Diffusion-based semantic image editing with mask guidance. In *ICLR*, 2023. [3](#)
- [14] Thomas Defard, Aleksandr Setkov, Angelique Loesch, and Romaric Audiger. Padim: A patch distribution modeling framework for anomaly detection and localization. In *Pattern Recognition. ICPR International Workshops and Challenges*, 2021. [2](#)
- [15] Jia Deng, Wei Dong, Richard Socher, Li-Jia Li, Kai Li, and Li Fei-Fei. Imagenet: A large-scale hierarchical image database. In *CVPR*, pages 248–255, 2009. [2, 3](#)
- [16] Prafulla Dhariwal and Alexander Nichol. Diffusion models beat gans on image synthesis. *NeurIPS*, 34:8780–8794, 2021. [2, 3, 4](#)
- [17] Matic Fučka, Vitjan Zavrtanik, and Danijel Skočaj. TransFusion – A Transparency-Based Diffusion Model for Anomaly Detection. In *ECCV*, 2024. [2](#)
- [18] Ian Goodfellow, Jean Pouget-Abadie, Mehdi Mirza, Bing Xu, David Warde-Farley, Sherjil Ozair, Aaron Courville, and Yoshua Bengio. Generative adversarial nets. In *NeurIPS*, pages 2672–2680, 2014. [2](#)
- [19] Jinjin Gu, Yujun Shen, and Bolei Zhou. Image processing using multi-code gan prior. In *CVPR*, 2020. [3](#)
- [20] Zhaopeng Gu, Bingke Zhu, Guibo Zhu, Yingying Chen, Hao Li, Ming Tang, and Jinqiao Wang. Filo: Zero-shot anomaly detection by fine-grained description and high-quality localization. In *ACM MM*, 2024. [2, 3, 6](#)
- [21] Denis Gudovskiy, Shun Ishizaka, and Kazuki Kozuka. Cflow-ad: Real-time unsupervised anomaly detection with localization via conditional normalizing flows. In *IEEE/CVF Win. Conf. App. Comput. Vis.*, pages 98–107, 2022. [2](#)
- [22] Haoyang He, Jiangning Zhang, Hongxu Chen, Xuhai Chen, Zhishan Li, Xu Chen, Yabiao Wang, Chengjie Wang, and Lei Xie. A diffusion-based framework for multi-class anomaly detection. In *AAAI*, pages 8472–8480, 2024. [2](#)
- [23] Kaiming He, Xiangyu Zhang, Shaoqing Ren, and Jian Sun. Deep residual learning for image recognition. In *CVPR*, pages 770–778, 2016. [2](#)
- [24] Amir Hertz, Ron Mokady, Jay Tenenbaum, Kfir Aberman, Yael Pritch, and Daniel Cohen-Or. Prompt-to-prompt image editing with cross-attention control. In *ICLR*, 2023. [2, 3](#)
- [25] Samet Hicsonmez, Abd El Rahman Shabayek, and Djamila Aouada. Vlmdiff: Leveraging vision-language models for multi-class anomaly detection with diffusion. In *IEEE/CVF Win. Conf. App. Comput. Vis.*, 2026. [2](#)
- [26] Jonathan Ho and Tim Salimans. Classifier-free diffusion guidance. In *NeurIPS 2021 Workshop on Deep Generative Models and Downstream Applications*, 2021. [4](#)
- [27] Jonathan Ho, Ajay Jain, and Pieter Abbeel. Denoising diffusion probabilistic models. In *NeurIPS*, pages 6840–6851, 2020. [2](#)
- [28] Jongheon Jeong, Yang Zou, Taewan Kim, Dongqing Zhang, Avinash Ravichandran, and Onkar Dabeer. Winclip: Zero-/few-shot anomaly classification and segmentation. In *CVPR*, 2023. [1, 2, 3, 6, 7](#)
- [29] Stepan Jezek, Martin Jonak, Radim Burget, Pavel Dvorak, and Milos Skotak. Deep learning-based defect detection of

metal parts: evaluating current methods in complex conditions. In *Int. Cong. on Ultra Modern Telecomm. and Control Sys. and Works.*, 2021. 7

[30] Alexander Kirillov, Eric Mintun, Nikhila Ravi, Hanzi Mao, Chloe Rolland, Laura Gustafson, Tete Xiao, Spencer Whitehead, Alexander C Berg, Wan-Yen Lo, et al. Segment anything. In *ICCV*, pages 4015–4026, 2023. 3

[31] Sungwook Lee, Seunghyun Lee, and Byung Cheol Song. CfA: Coupled-hypersphere-based feature adaptation for target-oriented anomaly localization. *IEEE Access*, 10: 78446–78454, 2022. 2

[32] Jiarui Lei, Xiaobo Hu, Yue Wang, and Dong Liu. Pyramid-flow: High-resolution defect contrastive localization using pyramid normalizing flow. In *CVPR*, pages 14143–14152, 2023. 2

[33] Xiaofan Li, Zhizhong Zhang, Xin Tan, Chengwei Chen, Yanyun Qu, Yuan Xie, and Lizhuang Ma. Promptad: Learning prompts with only normal samples for few-shot anomaly detection. In *CVPR*, pages 16838–16848, 2024. 1

[34] Yiting Li, Adam Goodge, Fayao Liu, and Chuan-Sheng Foo. Promptad: Zero-shot anomaly detection using text prompts. In *IEEE/CVF Win. Conf. App. Comput. Vis.*, pages 1093–1102, 2024. 1, 2, 6

[35] Yuanwei Li, Elizaveta Ivanova, and Martins Bruveris. Fade: Few-shot/zero-shot anomaly detection engine using large vision-language model. In *BMVC*, 2024. 6, 7

[36] Shilong Liu, Zhaoyang Zeng, Tianhe Ren, Feng Li, Hao Zhang, Jie Yang, Qing Jiang, Chunyuan Li, Jianwei Yang, Hang Su, et al. Grounding dino: Marrying dino with grounded pre-training for open-set object detection. In *ECCV*, pages 38–55. Springer, 2024. 3

[37] Zhihang Liu, Yiming Zhou, Yuansheng Xu, and Zilei Wang. Simplenet: A simple network for image anomaly detection and localization. In *CVPR*, pages 20402–20411, 2023. 2

[38] Chenlin Meng, Yutong He, Yang Song, Jiaming Song, Jiajun Wu, Jun-Yan Zhu, and Stefano Ermon. Sdedit: Guided image synthesis and editing with stochastic differential equations. In *ICLR*, 2022. 3

[39] Ron Mokady, Amir Hertz, Kfir Aberman, Yael Pritch, and Daniel Cohen-Or. Null-text inversion for editing real images using guided diffusion models. In *CVPR*, pages 6038–6047, 2023. 2, 3

[40] Paolo Napoletano, Flavio Piccoli, and Raimondo Schettini. Anomaly detection in nanofibrous materials by cnn-based self-similarity. *Sensors*, 18, 2018. 2

[41] Ken Perlin. An image synthesizer. *ACM Siggraph Computer Graphics*, 19(3):287–296, 1985. 2

[42] Zhen Qu, Xian Tao, Xinyi Gong, ShiChen Qu, Qiyu Chen, Zhengtao Zhang, Xingang Wang, and Guiguang Ding. Bayesian prompt flow learning for zero-shot anomaly detection. In *CVPR*, 2025. 6

[43] Alec Radford, Jong Wook Kim, Chris Hallacy, Aditya Ramesh, Gabriel Goh, Sandhini Agarwal, Girish Sastry, Amanda Askell, Pamela Mishkin, Jack Clark, Gretchen Krueger, and Ilya Sutskever. Learning transferable visual models from natural language supervision. In *ICML*, pages 8748–8763, 2021. 2

[44] Wei Ran, Zefang Yu, Suncheng Xiang, Ting Liu, and Yuzhuo Fu. A training-free correlation-weighted model for zero-/few-shot industrial anomaly detection with retrieval augmentation. In *ICASSP*, 2025. 6

[45] Robin Rombach, Andreas Blattmann, Dominik Lorenz, Patrick Esser, and Björn Ommer. High-resolution image synthesis with latent diffusion models. In *CVPR*, pages 10684–10695, 2022. 4

[46] Karsten Roth, Latha Pemula, Joaquin Zepeda, Bernhard Schölkopf, Thomas Brox, and Peter Gehler. Towards total recall in industrial anomaly detection. In *CVPR*, pages 14318–14328, 2022. 2

[47] Thomas Schlegl, Philipp Seeböck, Sebastian M Waldstein, Georg Langs, and Ursula Schmidt-Erfurth. f-anogan: Fast unsupervised anomaly detection with generative adversarial networks. *Medical image analysis*, 54:30–44, 2019. 2

[48] Eli Schwartz, Assaf Arbelle, Leonid Karlinsky, Sivan Harary, Florian Scheidegger, Sivan Doveh, and Raja Giryes. Maeday: Mae for few- and zero-shot anomaly-detection. *CVIU*, 241:103958, 2024. 1, 2, 3, 6

[49] Abd El Rahman Shabayek, Arunkumar Rathinam, Matthieu Ruthven, Djamila Aouada, and Tazdin Amietszajew. Ai-enabled thermal monitoring of commercial (phev) li-ion pouch cells with feature-adapted unsupervised anomaly detection. *Journal of Power Sources*, 2025. 2

[50] Jiaming Song, Chenlin Meng, and Stefano Ermon. Denoising diffusion implicit models. In *ICLR*, 2021. 2, 4

[51] Chengjie Wang, Wenbing Zhu, Bin-Bin Gao, Zhenye Gan, Jiangning Zhang, Zhihao Gu, Shuguang Qian, Mingang Chen, and Lizhuang Ma. Real-iad: A real-world multi-view dataset for benchmarking versatile industrial anomaly detection. In *CVPR*, pages 22883–22892, 2024. 1

[52] Shenzhi Wang, Liwei Wu, Lei Cui, and Yujun Shen. Glancing at the patch: Anomaly localization with global and local feature comparison. In *CVPR*, 2021. 2

[53] Xudong Wang, Rohit Girdhar, Stella X Yu, and Ishan Misra. Cut and learn for unsupervised object detection and instance segmentation. In *CVPR*, pages 3124–3134, 2023. 4, 5, 6

[54] Julia Wolleb, Florentin Bieder, Robin Sandkühler, and Philippe C Cattin. Diffusion models for medical anomaly detection. In *MICCAI*, pages 35–45, 2022. 2

[55] Zongze Wu, Dani Lischinski, and Eli Shechtman. Stylespace analysis: Disentangled controls for stylegan image generation. In *CVPR*, pages 12863–12872, 2021. 3

[56] Julian Wyatt, Adam Leach, Sebastian M Schmon, and Chris G Willcocks. Anodddpm: Anomaly detection with denoising diffusion probabilistic models using simplex noise. In *CVPRW*, pages 650–656, 2022. 2

[57] Vitjan Zavrtanik, Matej Kristan, and Danijel Skočaj. Draem: a discriminatively trained reconstruction embedding for surface anomaly detection. In *ICCV*, pages 8330–8339, 2021. 2, 6

[58] Hui Zhang, Zheng Wang, Zuxuan Wu, and Yu-Gang Jiang. Diffusionad: Norm-guided one-step denoising diffusion for anomaly detection. *arXiv preprint arXiv:2303.08730*, 2023. 2

- [59] Jiangning Zhang, Xuhai Chen, Yabiao Wang, Chengjie Wang, Yong Liu, Xiangtai Li, Ming-Hsuan Yang, and Dacheng Tao. Exploring plain vit reconstruction for multi-class unsupervised anomaly detection. *CVIU*, 2025. [2](#)
- [60] Tianrui Zhang, Liang Gao, Xinyu Li, and Yiping Gao. Dzad: Diffusion-based zero-shot anomaly detection. In *AAAI*, 2025. [6](#), [7](#)
- [61] Ximiao Zhang, Min Xu, and Xiuzhuang Zhou. Realnet: A feature selection network with realistic synthetic anomaly for anomaly detection. In *CVPR*, pages 16699–16708, 2024. [2](#)
- [62] Qihang Zhou, Guansong Pang, Yu Tian, Shibo He, and Jiming Chen. Anomalyclip: Object-agnostic prompt learning for zero-shot anomaly detection. In *ICLR*, 2024. [1](#), [2](#), [6](#)
- [63] Jiaqi Zhu, Shaofeng Cai, Fang Deng, Beng Chin Ooi, and Junran Wu. Do llms understand visual anomalies? uncovering llm’s capabilities in zero-shot anomaly detection. In *ACM MM*, pages 48–57, 2024. [3](#), [6](#), [1](#)
- [64] Jun-Yan Zhu, Philipp Krähenbühl, Eli Shechtman, and Alexei A Efros. Generative visual manipulation on the natural image manifold. In *ECCV*, pages 597–613. Springer, 2016. [3](#)
- [65] Yang Zou, Jongheon Jeong, Latha Pemula, Dongqing Zhang, and Onkar Dabeer. Spot-the-difference self-supervised pre-training for anomaly detection and segmentation. In *ECCV*, pages 392–408, 2022. [1](#), [5](#), [6](#)

6. Overview

In this supplementary material, we first present qualitative results of DIVAD on the MPDD dataset, as shown in Figure 7. We then provide detailed class-wise quantitative results across all three benchmark datasets.

On the MPDD dataset, DIVAD effectively localises various anomaly types, including *misplaced holes*, *defective paintings*, and *rust* across diverse object categories. These results highlight the robustness and broad applicability of our approach in handling heterogeneous industrial anomalies.

In Table 7, we provide a detailed class-wise comparison. We select two representative **training-free** ZSAD methods, FADE [63] and AnomalyVLM [9], for comparison, as (1) their official implementations are publicly available, and (2) they report state-of-the-art performance on at least one of the three benchmark datasets. To ensure a fair comparison, we reproduce their class-wise results using their official codebases. **Notably, we observed discrepancies between the results reported in the original papers and those obtained via their released implementations.** While we refer to the paper-reported numbers in the main text for consistency with prior work, here we report the values obtained through direct re-evaluation. **Importantly, these results show that our method achieves state-of-the-art performance across all pixel-level metrics, except for PRO, on the VISA dataset.**

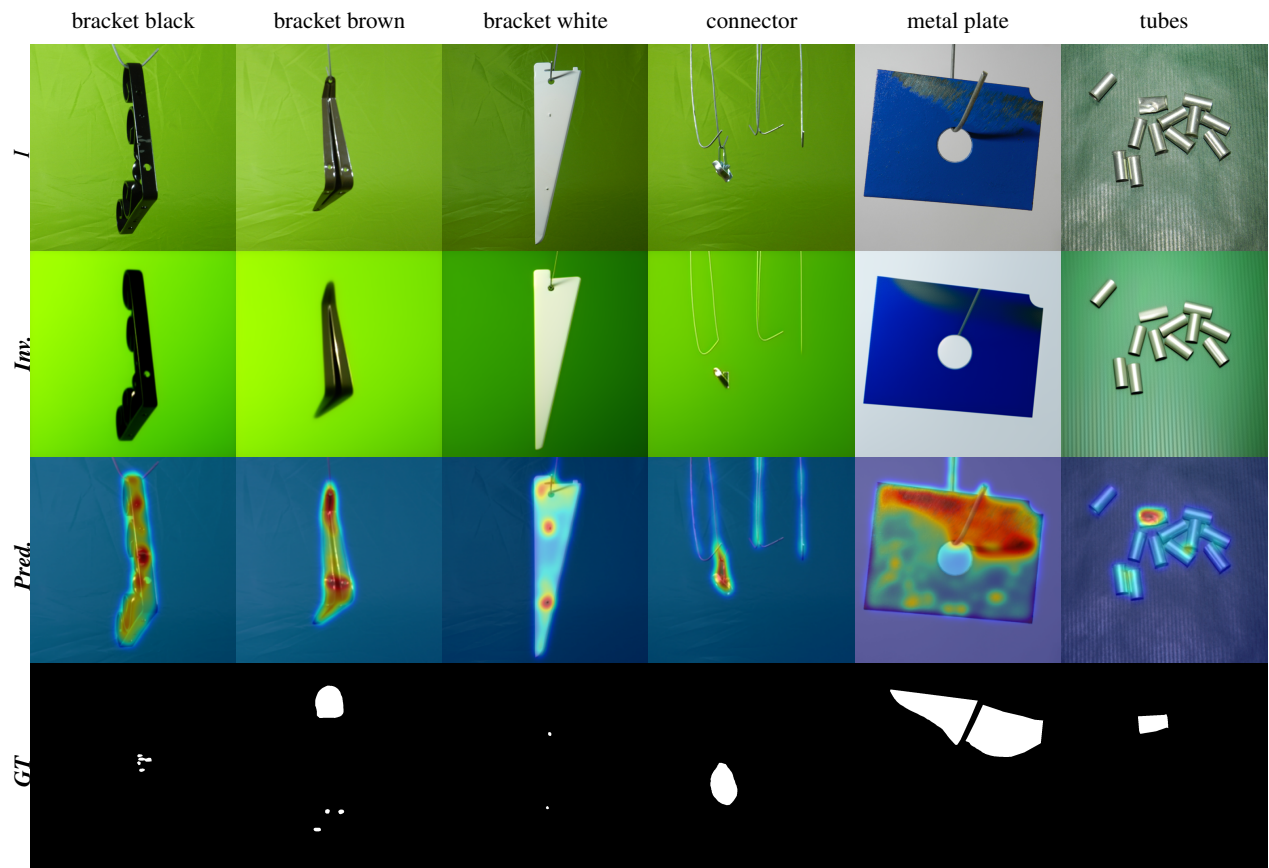


Figure 7. Visual results of DIVAD on MPDD. DIVAD successfully detects the anomaly locations on various objects with different anomaly types.

Table 7. Class-wise results on MVTec-AD (top), VISA (middle) and MPDD (bottom) datasets.

Dataset	Class	FADE [63]					AnomalyVLM [9]					DIVAD				
		ROC_I	ROC_P	PRO	AP_P	$F1_P$	ROC_I	ROC_P	PRO	AP_P	$F1_P$	ROC_I	ROC_P	PRO	AP_P	$F1_P$
MVTec-AD	bottle	97.9	89.2	79.6	48.9	50.6	79.3	69.0	39.5	32.6	39.3	86.4	85.1	63.3	42.5	44.3
	cable	85.1	78.4	68.0	13.0	20.9	55.0	69.1	33.6	19.9	32.3	62.4	75.4	54.7	9.1	18.1
	capsule	68.9	89.2	86.3	14.8	21.5	52.0	61.9	34.8	8.3	17.7	57.8	92.7	81.7	11.9	19.2
	hazelnut	91.4	97.3	92.0	44.1	47.5	83.9	85.5	59.9	38.8	44.8	57.1	87.6	66.6	13.6	18.4
	metalnut	95.9	70.8	69.7	21.2	30.5	28.9	60.0	23.9	13.3	36.2	61.7	72.9	50.4	23.7	36.0
	pill	81.1	84.8	84.8	15.5	21.3	40.4	93.2	64.6	51.7	45.6	61.9	82.4	65.1	11.2	18.4
	screw	72.4	97.8	91.2	17.9	26.0	40.6	67.6	28.5	6.8	20.8	66.1	95.8	75.9	6.1	12.3
	toothbrush	84.7	90.7	89.3	15.6	23.4	20.6	64.2	25.3	2.2	8.2	51.9	90.2	77.6	13.9	22.1
	transistor	87.5	61.4	55.3	11.8	19.5	31.0	64.9	26.3	6.7	19.6	70.4	71.6	38.8	9.2	17.8
	zipper	89.7	92.4	82.9	37.4	42.6	35.2	78.8	28.4	12.4	21.3	94.5	91.9	74.7	25.7	27.2
	carpet	99.3	99.3	97.8	75.1	72.2	94.8	70.2	37.1	39.6	56.4	99.8	98.7	96.2	76.0	71.1
	grid	99.5	98.3	94.7	38.4	47.2	80.5	63.9	42.7	12.4	18.2	100.0	99.3	97.5	60.8	59.1
	leather	100.0	99.3	98.2	45.7	52.3	98.2	85.2	74.8	64.6	72.7	97.5	99.0	97.9	54.3	57.2
	tile	99.9	92.3	79.5	47.0	53.6	96.3	81.6	63.5	61.7	64.8	89.7	92.6	76.9	57.0	56.0
	wood	97.5	97.2	91.6	65.0	67.7	98.8	81.8	53.9	60.3	67.2	82.9	93.5	83.0	59.0	58.3
	mean	90.1	89.2	84.1	34.1	39.8	62.4	73.1	42.4	28.8	37.7	76.0	88.6	73.3	31.6	35.7
VISA	candle	95.1	93.3	93.8	5.8	14.1	62.5	55.8	25.6	4.1	15.2	69.8	95.3	78.7	8.3	14.9
	capsules	80.4	80.5	42.5	4.2	11.0	62.4	85.1	52.2	31.9	41.6	57.7	94.5	86.4	32.2	39.0
	cashew	91.1	86.1	86.9	7.2	11.5	83.3	54.9	61.5	7.1	13.4	80.4	94.9	89.4	25.2	28.3
	chewinggum	95.0	99.1	90.3	35.7	47.0	92.6	93.8	52.6	31.3	36.1	87.0	97.7	77.5	65.4	63.8
	fryum	69.1	94.0	90.4	24.3	32.6	38.8	94.5	34.0	17.6	22.5	73.3	94.5	82.4	36.5	38.1
	macaroni1	78.9	98.3	80.2	8.6	18.0	82.4	81.0	27.7	19.2	26.1	76.4	97.0	89.2	20.0	28.2
	macaroni2	66.7	97.0	74.1	5.0	15.7	74.7	75.9	37.3	28.4	35.4	66.2	96.8	88.2	8.8	16.4
	pcb1	72.5	83.9	69.8	2.2	5.9	67.9	74.0	3.9	6.1	21.3	68.5	88.4	56.3	2.9	5.6
	pcb2	44.4	86.7	60.3	1.0	2.6	69.0	82.9	48.7	1.9	8.9	66.4	85.1	56.1	1.7	4.9
	pcb3	63.8	87.3	72.7	1.3	3.2	55.6	72.7	47.8	1.9	9.8	54.3	89.1	71.1	3.1	8.6
	pcb4	75.9	89.2	69.6	3.7	8.2	70.3	66.3	14.2	2.8	10.9	55.3	92.6	73.5	11.7	19.4
	pipe-fryum	62.8	96.9	94.8	21.1	32.1	93.1	72.4	37.5	13.0	24.5	81.4	95.0	90.0	18.0	21.2
	mean	74.7	91.0	77.1	10.0	16.8	71.1	75.8	36.9	13.8	22.1	69.7	93.4	78.2	19.5	24.0
MPDD	bracket black	39.8	93.7	80.8	1.0	2.6	67.8	89.4	31.8	1.1	2.8	51.7	95.8	80.6	2.2	5.0
	bracket brown	35.5	94.3	90.3	7.2	14.0	26.7	65.1	22.0	1.8	7.4	52.6	90.0	70.6	4.1	8.5
	bracket white	48.2	94.4	70.9	0.4	1.0	69.6	94.8	28.9	9.8	22.7	59.1	97.5	89.0	2.2	6.0
	connector	79.0	96.2	89.4	17.9	27.8	23.8	71.9	24.6	3.3	11.4	73.6	95.0	83.3	8.6	16.0
	metal plate	94.3	92.1	80.3	51.8	61.6	37.0	72.4	24.4	22.2	48.2	63.1	94.5	81.7	62.3	68.3
	tubes	80.1	94.8	80.0	35.3	40.9	78.0	74.7	35.3	7.1	16.2	80.4	96.6	86.6	58.1	58.3
	mean	62.8	94.2	83.9	18.9	24.6	50.5	78.0	27.8	7.5	18.1	63.4	94.9	82.0	22.9	27.0